A halide perovskite based ternary heterojunction with multi-shell hollow structure for stable and efficient artificial photosynthesis

You-Xiang Feng [a], Ke Su [a], Zhao-Lei Liu [a], Su-Xian Yuan [a], Yan-Fei Mu [b], Min Zhang [a,*], Tong-Bu Lu [a,*]

[a] MOE International Joint Laboratory of Materials Microstructure, Institute for New Energy Materials and Low Carbon Technologies, School of Materials Science and Engineering, Tianjin University of Technology, Tianjin 300384, China
[b] School of Chemistry and Chemical Engineering, Yangzhou University, Yangzhou, Jiangsu 225009, China

ARTICLE INFO

ABSTRACT

Low-cost halide perovskite materials hold great promise as photocatalysts for CO$_2$ reduction. However, their inferior water-tolerance will lead to a substantial decline in activity during prolonged photocatalytic CO$_2$ reduction with water as the electron source. Herein, we integrate a lead-free halide perovskite Cs$_3$Bi$_2$I$_9$ as photoactive layer with TiO$_2$ as water oxidation catalyst and g-C$_3$N$_4$ as CO$_2$ reduction catalyst to construct a ternary heterojunction (TiO$_2$/Cs$_3$Bi$_2$I$_9$/g-C$_3$N$_4$) with a multi-shell hollow structure. The formation of heterojunction endows TiO$_2$/Cs$_3$Bi$_2$I$_9$/g-C$_3$N$_4$ composite with enhanced photocatalytic activity for CO$_2$ reduction due to the improved photogenerated carrier separation. TiO$_2$/Cs$_3$Bi$_2$I$_9$/g-C$_3$N$_4$ achieves a CO yield of 120.6 μmol g^{-1} h^{-1} for photocatalytic CO$_2$ reduction, which is 3.1 times higher than that of individual Cs$_3$Bi$_2$I$_9$. More importantly, benefitting from the double-sided protection of g-C$_3$N$_4$ and TiO$_2$, the photocatalytic CO$_2$ reduction activity of TiO$_2$/Cs$_3$Bi$_2$I$_9$/g-C$_3$N$_4$ remains undiminished even over 100 h of continuous light irradiation, demonstrating significantly improved stability in water-contained reaction system.

1. Introduction

Photocatalytic CO$_2$ reduction, utilizing water as the electron donor, has the potential to convert and store the abundant energy of the sun in an eco-friendly and sustainable manner by mimicking plant photosynthesis, which has emerged as a promising pathway for achieving CO$_2$ recycling and garnered considerable attention over the past decade [1, 2]. Regrettably, the potential of this route is presently hindered by the inefficiency of the photocatalytic process [3,4], arising from sluggish kinetics of the water oxidation half-reaction with energy-uphill and multi-electron transfer pathway [5]. Conversely, the majority of highly efficient photocatalytic CO$_2$ reduction catalyst systems are inseparable from the employment of costly sacrificial agents [6–13]. In order to improve the photocatalytic performance of CO$_2$ conversion with water as the electron donor, numerous studies have focused on the strategies to improve the charge separation efficiency such as constructing heterojunctions, loading cocatalysts, surface/interface engineering, etc [14–22]. Furthermore, exploiting photocatalysts with broad spectral response and long photogenerated carrier lifetime is likewise a proven

avenue to enhance the efficiency of photocatalytic CO$_2$ reduction [23]. In this context, halide perovskite materials have emerged as an exceptionally promising category of photocatalysts in the recent years [24, 25], owing to their many captivating advantages, including cost-effectiveness, high absorption coefficient, tunable band structure, and long carrier lifetime [26,27].

In the field of photocatalytic CO$_2$ reduction, halide perovskite-based photocatalysts have achieved significant improvements in activity by combining halide perovskites with water oxidation catalysts (such as TiO$_2$, Bi$_2$WO$_6$, Fe$_2$O$_3$, etc.) [28–32] to construct binary Z-scheme heterojunctions. Nevertheless, the ionic crystal properties of halide perovskite materials contribute to their poor stability in water and polar solvents [33]. The majority of the constructed heterojunctions expose the halide perovskite to a watery environment, consequently diminishing the stability of the heterojunction catalysts (Scheme 1a). Embedding halide perovskite into water-resistant matrix (Scheme 1b) can effectively ameliorate the stability of halide perovskite-based photocatalyst in water-contained systems [34,35]. Nevertheless, this core-shell configuration also impedes the effective contact between CO$_2$ and

halide perovskite. Therefore, whether halide perovskite within this composite acts as a CO_2 reduction catalyst or a water oxidation catalyst, its overall catalytic performance will be constrained by the reduction or oxidation half-reaction occurring in the core layer. To conquer this dilemma, employing halide perovskite as the middle photoactive layer, the construction of a ternary heterojunction system with a sandwich structure by combining suitable water oxidation and CO_2 reduction catalysts on both sides (Scheme 1c) should be a feasible tactic, which not only avoid contact between the inner halide perovskite and H_2O but also improve the efficiency of photogenerated charge separation. Nevertheless, as far as our knowledge extends, there has been no report of a halide perovskite-based ternary heterojunction employed for photocatalytic CO_2 reduction to date, because the environmental sensitivity of halide perovskites poses challenges in depositing catalysts on their surfaces.

To demonstrate this concept, herein we present a lead-free halide perovskite $Cs_3Bi_2I_9$ based ternary heterojunction through the integration of titania (TiO_2) and graphitic carbon nitride (g-C_3N_4). The sacrificial template method was adopted to confer a multi-shell hollow structure upon the prepared ternary heterojunction TiO_2/$Cs_3Bi_2I_9$/g-C_3N_4, which facilitates the contact between the reaction substrate and both the inner and outer surfaces of the catalyst. It is noteworthy that the middle layer of $Cs_3Bi_2I_9$ primarily serves as a light absorber within this structure. TiO_2 has been demonstrated to form a Z-scheme heterojunction with halide perovskite [30], thus the photogenerated holes in TiO_2 are preserved for completing the water oxidation reaction. Loading halide perovskite onto g-C_3N_4 can creates a conventional type-II heterojunction [36], allowing the rapid transfer of photogenerated electrons from $Cs_3Bi_2I_9$ to the conduction band of g-C_3N_4 for participating in the CO_2 reduction reaction. The dual built-in electric fields formed among these three components provide a robust driving force for effective charge separation. Consequently, TiO_2/$Cs_3Bi_2I_9$/g-C_3N_4 exhibits significantly enhanced photocatalytic activity without the need for any organic electron sacrificial agents. The CO yield of photocatalytic CO_2 reduction reaches up 120.6 μmol g^{-1} h^{-1}, surpassing the individual components by a significant margin. More importantly, the unique sandwich configuration prevents direct contact between $Cs_3Bi_2I_9$ and water, thereby greatly enhancing the stability of the composite catalyst. The photocatalytic activity of the ternary heterojunction shows no sign of deterioration even after continuous illumination over 100 h.

2. Experimental section

2.1. Chemicals

Cesium iodide (CsI, 99.99%) was purchased from Xi'an Polymer Light Technology Corp. Ethanol (99.8%), isopropanol (IPA, 99.7%), tetrabutylammonium hexafluorophosphate (TBAPF$_6$, 98%), acetonitrile (99.8%), methanol (CH$_3$OH, 99.8%, $H_2O \leq 100$ ppm), titanium butoxide (TBO, 99%), cyanamide (50% in H_2O) and sodium hydroxide (NaOH, 98%) were acquired from Aladdin. Bismuth nitrate pentahydrate (Bi(NO$_3$)$_3$·5 H_2O, 99.9%), $^{13}CO_2$ and $H_2^{18}O$ were obtained from Energy Chemical. Tetraethyl orthosilicate (TEOS, 99%), ammonium hydroxide (NH$_3$·H_2O, 28%), ethylene glycol (EG, 99%), 5,5-dimethyl-1-pyrroline N-oxide (DMPO, 98%), 2,2,6,6-tetramethylpiperidine-1-oxyl (TEMPO, 98%) were sourced from Adamas. Hydriodic acid (HI, 57 wt % aqueous) was procured from ACROS. Methenamine (C$_6$H$_{12}$N$_4$, 99%) was purchased from Sinopharm Chemical Reagent Co. Ltd. It should be noted that all chemicals were commercially available and utilized without any additional purification.

2.2. Sample preparation

Preparation of SiO_2 microspheres: The SiO_2 microspheres were synthesized according to the previously reported procedure [37]. Briefly, a mixture of ethanol and water (V:V = 5:1, 120 mL) was added into a round-bottomed flask along with 2.0 mL of NH$_3$·H_2O (28 wt%). The resulting mixture was stirred for 30 min. Subsequently, 1.0 mL of TEOS was added drop by drop into the reaction system, and continuous stirring was maintained at room temperature for 8 h. Finally, the SiO_2 microspheres white powder can be obtained through centrifugation and subsequent freeze-drying.

Preparation of SiO_2/TiO_2 microspheres: The SiO_2/TiO_2 microspheres were synthesized through a TBO hydrolysis process [38]. Specifically, SiO_2 microspheres (200 mg) were combined with ethanol (45 mL) and NH$_3$·H_2O (200 μL, 28 wt%) in a 100 mL round-bottom flask. The mixture was sonicated for 30 min, followed by stirring for 1.5 h at 30 °C in a water bath. Subsequently, 6 mL solution of TBO in ethanol (V:V = 1:5) was added dropwise into the above mixture at 50 °C, then heated to 85 °C and held at this temperature for 2.5 h. The SiO_2/TiO_2 microspheres can be obtained through centrifugation and subsequent drying. Finally, a high crystalline sample can be obtained by annealing at 450 °C for 2 h.

Preparation of SiO_2/TiO_2/Bi_2O_3 microspheres: As-prepared SiO_2/
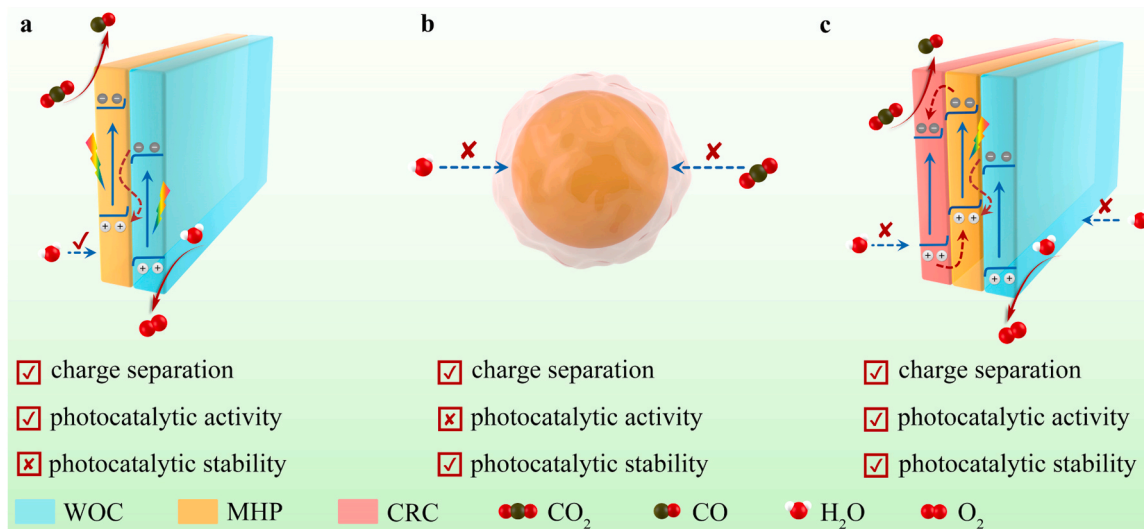
Scheme 1. a) Binary Z-scheme heterojunction composed of metal halide perovskite (MHP) and water oxidation catalyst (WOC). b) Core/shell structure composed of MHP core and CO_2 reduction catalyst (CRC) shell. c) MHP-based ternary heterojunction with a sandwich structure.

TiO$_2$ microspheres (100 mg), ethanol (20 mL), EG (1 mL), methenamine (20 mg) and Bi(NO$_3$)$_3$·5 H$_2$O (100 mg) were combined in a round-bottom flask. The mixture was stirred for 12 h at 60 ℃ in a water bath. Following centrifugation and subsequent washing with deionized water and ethanol, the SiO$_2$/TiO$_2$/Bi$_2$O$_3$ microspheres can be obtained through annealing at 450 ℃ for 2 h.

Preparation of SiO$_2$/TiO$_2$/Bi$_2$O$_3$/g-C$_3$N$_4$ microspheres: The SiO$_2$/TiO$_2$/Bi$_2$O$_3$/g-C$_3$N$_4$ microspheres were synthesized through a thermal polymerization process as outlined in reference [39]. Typically, SiO$_2$/-TiO$_2$/Bi$_2$O$_3$ microspheres (100 mg) were initially redispersed in a mixed solvent comprising ethanol (10 mL) and cyanamide (0.6 mL). This mixture was subjected to 30 min of ultrasonication, followed by stirring at 80 ℃ until the solvent completely evaporated. Subsequently, the SiO$_2$/TiO$_2$/Bi$_2$O$_3$/g-C$_3$N$_4$ microspheres can be obtained after annealing at 550 ℃ for 2 h. Hollow TiO$_2$/Bi$_2$O$_3$/g-C$_3$N$_4$ were prepared by etching SiO$_2$/TiO$_2$/Bi$_2$O$_3$/g-C$_3$N$_4$ in 10 mL of 2 M NaOH solution at 85 ℃ for 2 h.

Preparation of hollow TiO$_2$/Cs$_3$Bi$_2$I$_9$/g-C$_3$N$_4$ microspheres: Hollow TiO$_2$/Bi$_2$O$_3$/g-C$_3$N$_4$ microspheres (20 mg), CsI (20 mg), CH$_3$OH (10 mL) and HI (100 μL) were added into a round-bottom flask and stirred for 2 h at room temperature. Subsequently, the resulting hollow TiO$_2$/Cs$_3$Bi$_2$I$_9$/g-C$_3$N$_4$ microspheres were collected through centrifugation and washing with IPA to eliminate residual ions.

Preparation of hollow TiO$_2$/Cs$_3$Bi$_2$I$_9$ and Cs$_3$Bi$_2$I$_9$/g-C$_3$N$_4$ microspheres: The preparation of hollow TiO$_2$/Cs$_3$Bi$_2$I$_9$ and Cs$_3$Bi$_2$I$_9$/g-C$_3$N$_4$ microspheres followed a similar method to that of TiO$_2$/Cs$_3$Bi$_2$I$_9$/g-C$_3$N$_4$ microspheres, with the exception that cyanamide or TBO was not added, respectively.

Preparation of hollow TiO$_2$/g-C$_3$N$_4$ microspheres: The SiO$_2$/TiO$_2$ microspheres (100 mg) were initially dispersed in a mixed solvent comprising ethanol (10 mL) and cyanamide (0.6 mL). This mixture underwent 30 min of ultrasonication, followed by stirring at 80 ℃ until the solvent completely evaporated. Subsequently, the SiO$_2$/TiO$_2$/g-C$_3$N$_4$ microspheres were obtained after annealing at 550 ℃ for 2 h. Hollow TiO$_2$/g-C$_3$N$_4$ can be generated by etching SiO$_2$/TiO$_2$/g-C$_3$N$_4$ in 10 mL of 2 M NaOH solution at 85 ℃ for 2 h.

3. Results and discussion

3.1. Synthesis and structure characterizations

TiO$_2$/Cs$_3$Bi$_2$I$_9$/g-C$_3$N$_4$ ternary heterojunction was prepared via the template method of continuous deposition combined with *in situ* conversion. The schematic procedure is illustrated in Fig. 1a, and the detailed synthesis processes are described in the section of experimental section. In brief, colloidal SiO$_2$ microspheres obtained through the Stöber method [37] were selected as templates. Initially, an amorphous layer of TiO$_x$ was coated onto the surface of SiO$_2$ microspheres with tetrabutyl titanate as precursor through a sol-gel method [38], followed by calcination at 450 °C for 2 h to improve the crystallinity to obtain SiO$_2$/TiO$_2$. Given that halide perovskites are prone to decompose in polar solvents, a stable layer of Bi$_2$O$_3$ was subsequently deposited on the surface of TiO$_2$ as a precursor for the halide perovskite through Bi (NO$_3$)$_3$·5 H$_2$O hydrolysis to generate SiO$_2$/TiO$_2$/Bi$_2$O$_3$. Thereafter, a layer of g-C$_3$N$_4$ was coated onto the SiO$_2$/TiO$_2$/Bi$_2$O$_3$ surface with cyanamide as the raw material via thermal polymerization [39] to obtain SiO$_2$/TiO$_2$/Bi$_2$O$_3$/g-C$_3$N$_4$. TiO$_2$/Bi$_2$O$_3$/g-C$_3$N$_4$ microspheres with a hollow structure can be generated by etching the SiO$_2$ with a NaOH
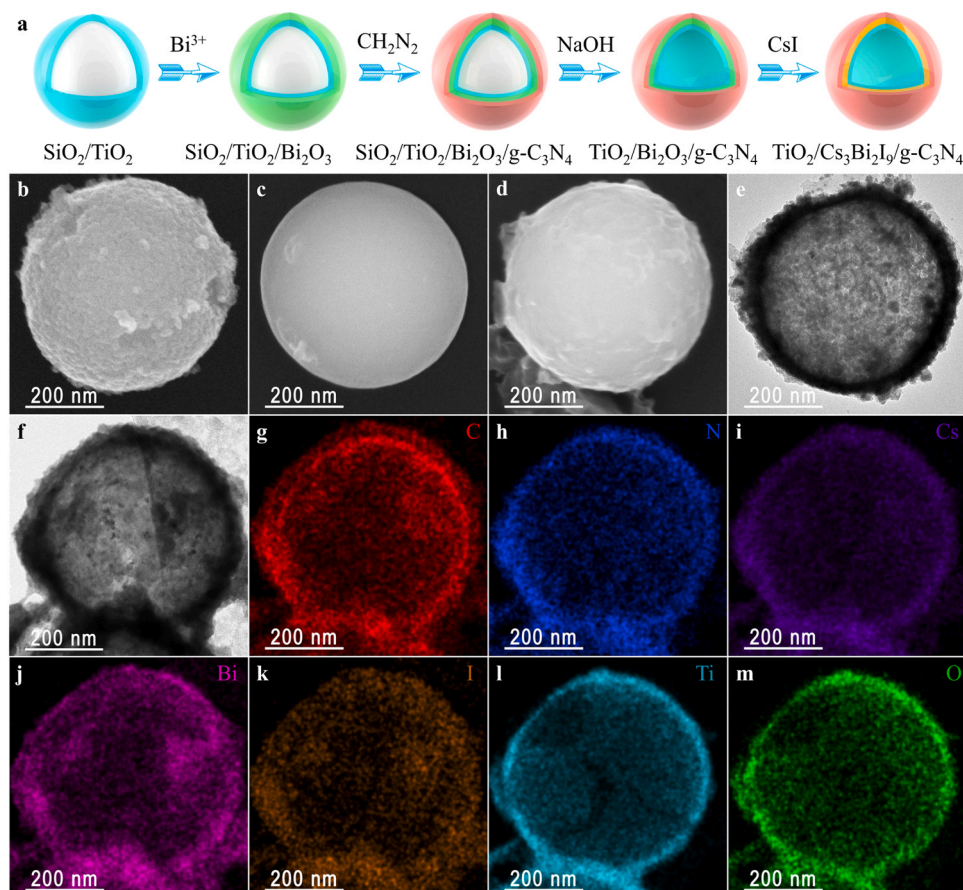
Fig. 1. a) Schematic illustration of the synthesis process of TiO$_2$/Cs$_3$Bi$_2$I$_9$/g-C$_3$N$_4$. b−d) HRSEM images of b) SiO$_2$/TiO$_2$, c) SiO$_2$/TiO$_2$/Bi$_2$O$_3$ and d) SiO$_2$/TiO$_2$/ Bi$_2$O$_3$/g-C$_3$N$_4$. e) TEM image of TiO$_2$/Bi$_2$O$_3$/g-C$_3$N$_4$. f) HRTEM image of TiO$_2$/Cs$_3$Bi$_2$I$_9$/g-C$_3$N$_4$. g−m) EDS elemental mapping images of TiO$_2$/Cs$_3$Bi$_2$I$_9$/g-C$_3$N$_4$ composite: g) C, h) N, i) Cs, j) Bi, k) I, l) Ti, and m) O.

solution. Finally, CsI was introduced to convert Bi_2O_3 into $Cs_3Bi_2I_9$ with the assistance of HI [40], resulting in the formation of $TiO_2/Cs_3Bi_2I_9/g-C_3N_4$ composites.

The morphologies of the prepared ternary heterojunction and its intermediates during the formation process were initially investigated by means of high-resolution scanning electron microscopy (HRSEM) and transmission electron microscopy (TEM). HRSEM image (Fig. S1) of the SiO_2 templates reveals a uniform microsphere structure with a smooth surface and a diameter of about 530 nm. A relatively rough layer of TiO_2 can be formed on the surface of SiO_2 microsphere by hydrolysis of tetrabutyl titanate as observed in Fig. 1b. Through the gradual hydrolysis of $Bi(NO_3)_3·5 H_2O$, a dense layer of Bi_2O_3 can be observed covering the surface of TiO_2/SiO_2 microsphere (Fig. 1c). After the deposition of g-C_3N_4, the resultant $SiO_2/TiO_2/Bi_2O_3/g-C_3N_4$ microsphere exhibits a rough surface (Fig. 1d). TEM was employed to investigate the morphology of $SiO_2/TiO_2/Bi_2O_3/g-C_3N_4$ treated with NaOH solution. As presented in Fig. 1e, the sample exhibits distinct hollow spherical structure, signifying the successful etching of the SiO_2 microspheres at the core position by NaOH. Additionally, the high-resolution TEM (HRTEM) image of $TiO_2/Cs_3Bi_2I_9/g-C_3N_4$ (Fig. 1f) reveals that the transformation of $TiO_2/Bi_2O_3/g-C_3N_4$ into $TiO_2/Cs_3Bi_2I_9/g-C_3N_4$ still maintains the original hollow microsphere morphology, suggesting that the transformation process does not result in the structural dissociation. Energy-dispersive X-ray spectroscopy (EDS) mapping measurements (Fig. 1g−m) demonstrate that of all the C, N, Cs, Bi, I, Ti, and O elements are uniformly distributed within the hollow microsphere, preliminarily confirming the successful preparation of multi-shell $TiO_2/Cs_3Bi_2I_9/g-C_3N_4$ microspheres with hollow structure.

Powder X-ray diffraction (PXRD) measurements were further conducted to inspect the compositions of the prepared ternary heterojunction. The XRD pattern of the SiO_2 microsphere displays a faint, broad and diffuse diffraction peak (Fig. S2), indicating the low crystallinity of the as-prepared SiO_2. As presented in Fig. 2a, TiO_2 coated on the surface of SiO_2 exhibits typical diffraction peaks characteristic of anatase TiO_2, closely matching the standard pattern of JCPDS: 21−1272. The XRD pattern of $SiO_2/TiO_2/Bi_2O_3$ displays prominent diffraction peaks of tetragonal Bi_2O_3 (JCPDS: 78−1793), which masks the characteristic peaks of TiO_2 in $SiO_2/TiO_2/Bi_2O_3$. Similarly, in the XRD pattern of $SiO_2/TiO_2/Bi_2O_3/g-C_3N_4$, only the diffraction peak of Bi_2O_3 is detectable, owing to the weak crystallinity of g-C_3N_4, which conceals its diffraction peak. Moreover, after the conversion of $TiO_2/Bi_2O_3/g-C_3N_4$ to $TiO_2/Cs_3Bi_2I_9/g-C_3N_4$, the corresponding XRD pattern solely displays the characteristic peak of the hexagonal phase $Cs_3Bi_2I_9$ due to the effect of the strong signals of $Cs_3Bi_2I_9$, which is consistent with its standard pattern of JCPDS: 73−0707. It is worth noting that the XRD patterns of individual TiO_2 and g-C_3N_4 remain unchanged after treatment with NaOH and HI (Fig. S3), indicating that neither TiO_2 nor g-C_3N_4 undergo decomposition during the etching of SiO_2 and the transformation of Bi_2O_3.

Fourier transform infrared spectroscopy (FTIR) and Raman spectroscopy measurements were further carried out to affirm the presence of TiO_2 and g-C_3N_4 in the ternary composites or binary composites. As depicted in Fig. 2b, the characteristic absorption peak at 466 cm^{-1} is evident in the FTIR spectrum of TiO_2, which can be attributed to the stretching vibration of O−Ti−O [41]. The FTIR spectrum of g-C_3N_4 exhibits clear peaks at 807 cm^{-1} and 1200–1600 cm^{-1}, corresponding to the bending vibration of triazine ring and stretching vibration of aromatic triazine heterocycles [42], respectively. Individual $Cs_3Bi_2I_9$ does not exhibit an IR spectral response within the observed window. The characteristic peaks of TiO_2 and g-C_3N_4 are clearly discernible in $TiO_2/Cs_3Bi_2I_9$ and $Cs_3Bi_2I_9/g-C_3N_4$ binary heterojunctions (Fig. S4), respectively. Moreover, both the characteristic peaks of TiO_2 and g-C_3N_4 are distinctly observable in the FTIR spectrum of the $TiO_2/Cs_3Bi_2I_9/g-C_3N_4$ ternary heterojunction. Fig. 2c and Fig. S5, displays the Raman spectra of single component, binary and ternary composites. Distinct characteristic peaks can be observed in the Raman spectrum of TiO_2 at 148 cm^{-1} and 401 cm^{-1}, which originate from the symmetric stretching vibration and the symmetric bending vibration O−Ti−O [43], respectively. Characteristic peaks related to the bridging Bi−I stretching vibration (101 cm^{-1}) and terminal Bi−I stretching vibration (149 cm^{-1}) are clearly discernible in the Raman spectrum of $Cs_3Bi_2I_9$ [44]. g-C_3N_4 has no distinct characteristic signals in its Raman spectra due to its own strong fluorescence effect [45]. The characteristic signals of both TiO_2 and $Cs_3Bi_2I_9$ are present in the Raman spectrum of $TiO_2/Cs_3Bi_2I_9/g-C_3N_4$. In addition, the Raman spectrum of $TiO_2/Cs_3Bi_2I_9$ reveals the typical Raman signals of both TiO_2 and $Cs_3Bi_2I_9$, and the characteristic signal of $Cs_3Bi_2I_9$ can also been observed in the Raman spectrum of $Cs_3Bi_2I_9/g-C_3N_4$. These results further confirm the successful preparation of the $TiO_2/Cs_3Bi_2I_9/g-C_3N_4$ ternary heterojunction.

3.2. Energy band structures and interfacial interaction

The energy band structures of the components in the $TiO_2/Cs_3Bi_2I_9/g-C_3N_4$ ternary heterojunction were examined by combining UV−visible diffuse reflectance spectroscopy (UV−Vis DRS) with ultraviolet photoelectron spectroscopy (UPS) measurements. As depicted in Fig. 3a, both TiO_2 and g-C_3N_4 exhibit relatively weak photon responses in the visible region, with absorption edges at approximately 384 nm and 445 nm, respectively, which result in a limited light-harvesting capacity for the $TiO_2/g-C_3N_4$ heterojunction. Notably, $Cs_3Bi_2I_9$ displays a broad spectral response range, with an absorption edge around 617 nm. The good light-harvesting capability of $Cs_3Bi_2I_9$ enables both the ternary heterojunction ($TiO_2/Cs_3Bi_2I_9/g-C_3N_4$) and the binary heterojunctions ($TiO_2/Cs_3Bi_2I_9$ and $Cs_3Bi_2I_9/g-C_3N_4$) to possess a strong response to visible light (Fig. 3a). By transforming the UV−Vis DRS spectra into the corresponding Tauc plots (Figs. S6a−c), the optical band gaps (E_g) of TiO_2, $Cs_3Bi_2I_9$ and g-C_3N_4 can be determined to be 3.15, 1.94, and 2.77 eV, respectively, which are consistent with previous reports [46–48]. Based

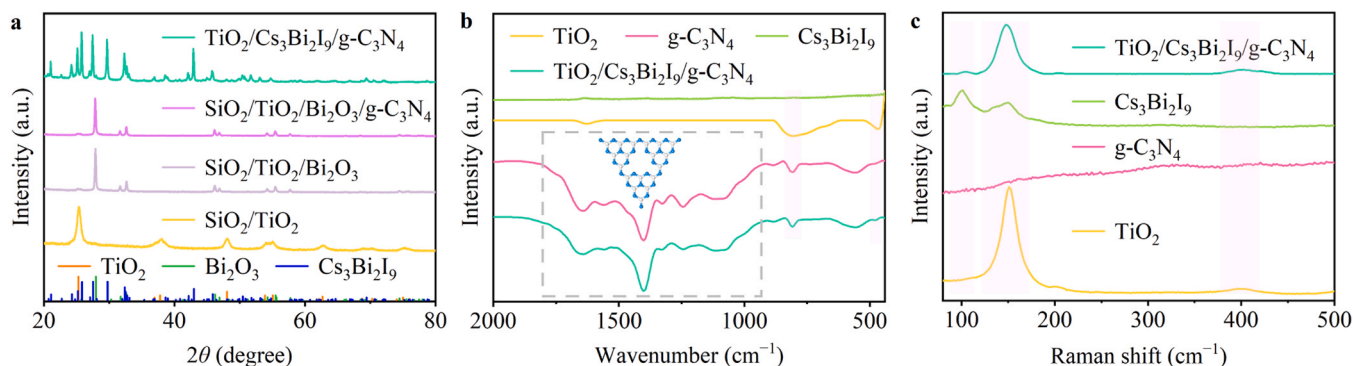**Fig. 2.** a) XRD patterns of SiO_2/TiO_2, $SiO_2/TiO_2/Bi_2O_3$, $SiO_2/TiO_2/Bi_2O_3/g-C_3N_4$ and $TiO_2/Cs_3Bi_2I_9/g-C_3N_4$. b) FTIR spectra of TiO_2, $Cs_3Bi_2I_9$, g-C_3N_4 and $TiO_2/Cs_3Bi_2I_9/g-C_3N_4$. c) Raman spectra of TiO_2, $Cs_3Bi_2I_9$, g-C_3N_4 and $TiO_2/Cs_3Bi_2I_9/g-C_3N_4$.
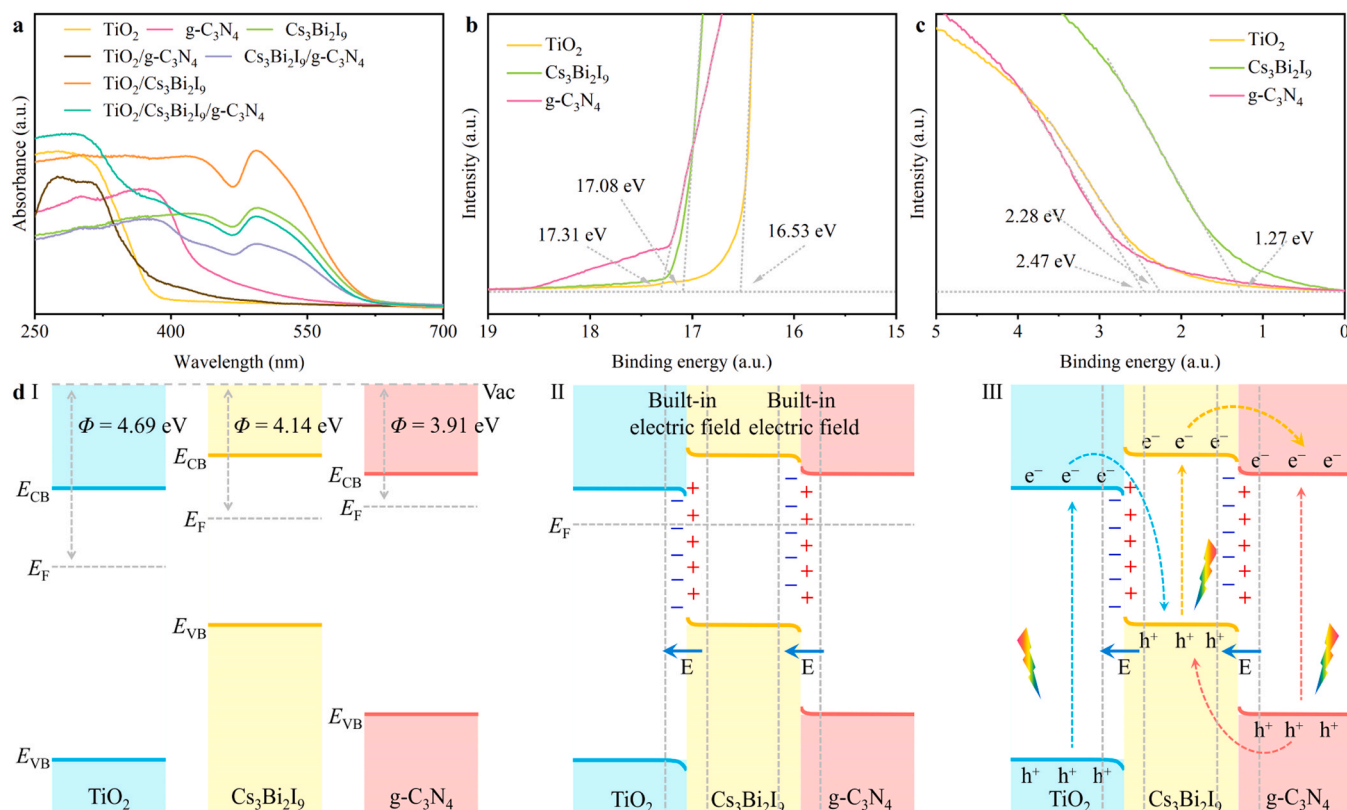
Fig. 3. a) UV−Vis DRS spectra of TiO_2, $Cs_3Bi_2I_9$, $g-C_3N_4$, $TiO_2/g-C_3N_4$, $Cs_3Bi_2I_9/g-C_3N_4$, $TiO_2/Cs_3Bi_2I_9$ and $TiO_2/Cs_3Bi_2I_9/g-C_3N_4$. b−c) UPS spectra of TiO_2, $Cs_3Bi_2I_9$ and $g-C_3N_4$ in the b) cutoff and c) onset energy regions. d) Energy band structure and charge transfer in $TiO_2/Cs_3Bi_2I_9/g-C_3N_4$: Energy band structures of TiO_2, $Cs_3Bi_2I_9$, and $g-C_3N_4$ before I) and after II) contact; III) Charge transfer pathway in $TiO_2/Cs_3Bi_2I_9/g-C_3N_4$ under illumination. Φ denotes the work function, and its value is the negative counterpart of the corresponding Fermi energy level (E_F).

on the ultraviolet photoelectron spectra (UPS) of TiO_2, $Cs_3Bi_2I_9$ and $g-C_3N_4$ in Fig. 3b and c, their valence band edge potentials (E_{VB}) can be calculated as 2.74, 0.91, and 1.88 V vs. the normal hydrogen electrode (NHE), respectively. According to the values of E_g and E_{VB}, the conduction band edge potentials (E_{CB}) of TiO_2, $Cs_3Bi_2I_9$, and $g-C_3N_4$ can be deduced as −0.68, −1.00, and −0.89 V (*vs.* NHE), respectively. In addition, the flat band potentials of TiO_2, $Cs_3Bi_2I_9$ and $g-C_3N_4$ were determined through Mott−Schottky curve measurements (Figs. S7a−c), being −0.65, −1.04, and −0.89 V *vs.* NHE, respectively, which align with the results of UPS measurements. The resultant energy band structures of TiO_2, $Cs_3Bi_2I_9$ and $g-C_3N_4$ are visualized in Fig. 3d (I). It is evident that there are staggered energy band alignments between $Cs_3Bi_2I_9$ and both TiO_2 and $g-C_3N_4$ in the $TiO_2/Cs_3Bi_2I_9/g-C_3N_4$ ternary heterojunction.

Furthermore, the Fermi energy levels (E_F) of TiO_2, $Cs_3Bi_2I_9$ and $g-C_3N_4$ can also be determined through UPS measurements as depicted in Fig. 3d (I), which are located at −4.69, −4.14, and −3.91 eV vs. vacuum, respectively. Their relative positions within the energy band structure are also visually represented in Fig. 3d (I). The disparity in E_F will give rise to interfacial free electron transfer when these materials come into close contact, ultimately achieving a unified E_F for the system. In the case of the $TiO_2/Cs_3Bi_2I_9$ interface, the E_F of $Cs_3Bi_2I_9$ surpasses than that of TiO_2, leading to the occurrence of free electron transfer from $Cs_3Bi_2I_9$ to TiO_2, which results in the establishment of a built-in electric field pointing from $Cs_3Bi_2I_9$ to TiO_2 as illustrated in Fig. 3d (II). At the $Cs_3Bi_2I_9/g-C_3N_4$ interface, the E_F of $Cs_3Bi_2I_9$ is lower than that of $g-C_3N_4$, prompting interfacial free electrons to flow from $g-C_3N_4$ to $Cs_3Bi_2I_9$, thus creating a built-in electric field directed from $g-C_3N_4$ to $Cs_3Bi_2I_9$ as presented in Fig. 3d (II).

The migration of interfacial free electron during heterojunction formation can be further confirmed by analyzing the shifts in the binding

energies of the constituent elements using high-resolution XPS measurements. As depicted in Fig. 4a−c, the binding energies of Cs 3*d*, Bi 4 *f*, and I 3*d* in the $TiO_2/Cs_3Bi_2I_9$ heterojunction all exhibit perceptibly shifts toward higher energies, approximately 0.20–0.39 eV higher than those in $Cs_3Bi_2I_9$ alone. In contrast, compared to pure TiO_2, the binding energies of Ti $2p_{3/2}$, Ti $2p_{1/2}$ and O 1*s* in the $TiO_2/Cs_3Bi_2I_9$ heterojunction are shifted to lower energies by 0.27, 0.29 and 0.22 eV, respectively (Fig. 4d and e). These results provide concrete evidence of free electron transfer from $Cs_3Bi_2I_9$ to TiO_2 upon the formation of the heterojunction. For the $Cs_3Bi_2I_9/g-C_3N_4$ heterojunction, all the binding energies of Cs 3*d*, Bi 4*f*, and I 3*d* are shifted toward lower energies by 0.08–0.49 eV compared to those in individual $Cs_3Bi_2I_9$ (Fig. 4a−c). Additionally, the binding energy of N 1*s* is shifted toward higher energies by 0.15–0.27 eV with respect to that of $g-C_3N_4$ alone (Fig. 4f). These outcomes confirm that electron transfer from $g-C_3N_4$ to $Cs_3Bi_2I_9$ takes place when they are in close proximity. Moreover, the perceivable shifts in the binding energies of these elements also underscore a robust interfacial electronic coupling among TiO_2, $Cs_3Bi_2I_9$ and $g-C_3N_4$ upon the formation of heterojunction, which will be favorable for the efficient separation of photogenerated carriers.

For the $TiO_2/Cs_3Bi_2I_9/g-C_3N_4$ ternary heterojunction, the binding energies of Cs 3*d*, Bi 4*f*, and I 3*d* are consistently shifted towards lower energies by 0.32–0.43 eV (Fig. 4a−c and Fig. S8a) in comparison to those in the $TiO_2/Cs_3Bi_2I_9$ binary heterojunction, while the binding energy of N 1*s* is elevated by 0.15–0.27 eV compared to that in individual $g-C_3N_4$, providing further evidence of the migration of free electrons from $g-C_3N_4$ to $Cs_3Bi_2I_9$ upon coating $g-C_3N_4$ layer onto the $TiO_2/Cs_3Bi_2I_9$ surface. Additionally, all the binding energies of Cs 3*d*, Bi 4*f*, and I 3*d* in the $TiO_2/Cs_3Bi_2I_9/g-C_3N_4$ ternary heterojunction are shifted towards higher energies by 0.09–0.32 eV relative to those in the $Cs_3Bi_2I_9/g-C_3N_4$ binary heterojunction, (Fig. 4 and Fig. S8b).
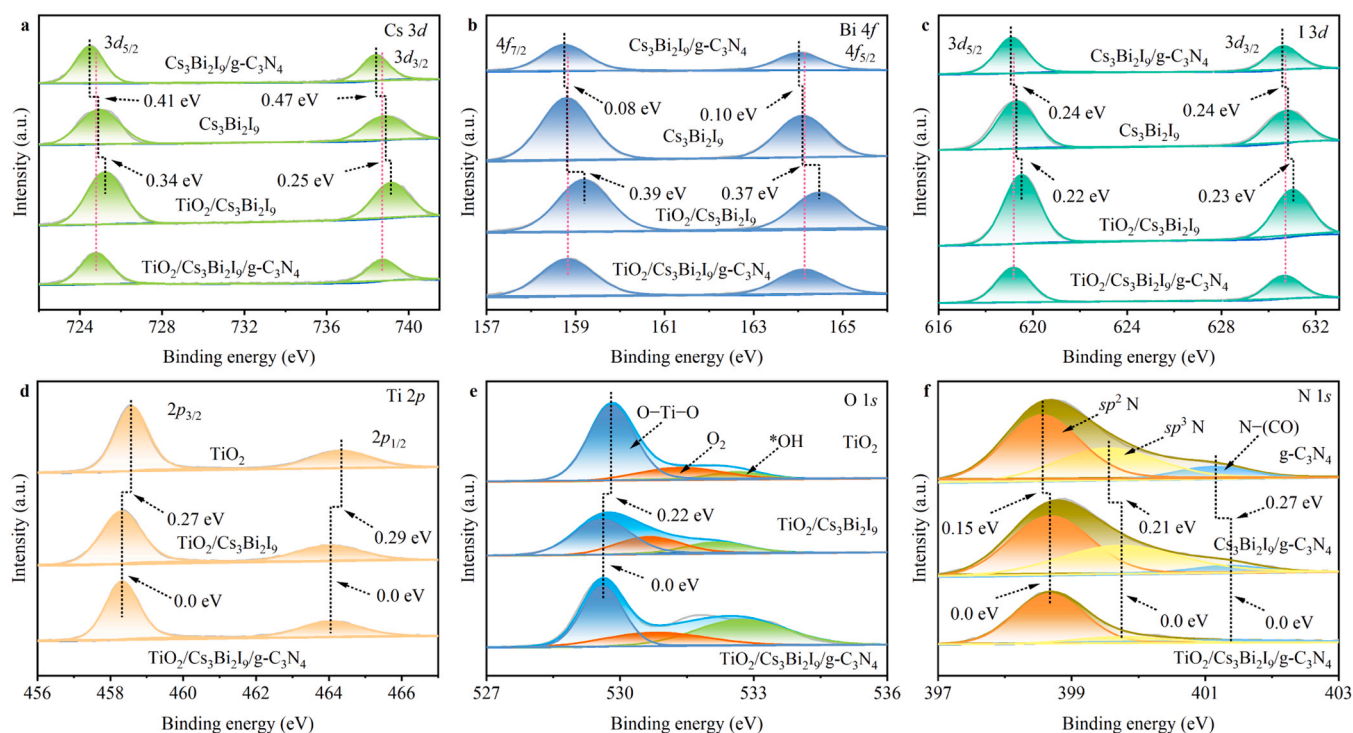
Fig. 4. a−c) High-resolution XPS spectra of a) Cs 3*d*, b) Bi 4*f* and c) I 3*d* in $Cs_3Bi_2I_9$, $TiO_2/Cs_3Bi_2I_9$, $Cs_3Bi_2I_9/g$-C_3N_4 and $TiO_2/Cs_3Bi_2I_9/g$-C_3N_4. d and e) High-resolution XPS spectra of d) Ti 2*p*, e) O 1*s* in TiO_2, $TiO_2/Cs_3Bi_2I_9$ and $TiO_2/Cs_3Bi_2I_9/g$-C_3N_4. f) High-resolution XPS spectra of N 1*s* in g-C_3N_4, $Cs_3Bi_2I_9/g$-C_3N_4 and $TiO_2/Cs_3Bi_2I_9/g$-C_3N_4.

Meanwhile, the binding energies of Ti 2*p* and O 1*s* in the $TiO_2/Cs_3Bi_2I_9/$ g-C_3N_4 ternary heterojunction are reduced by 0.22–0.29 eV in comparison to those in individual TiO_2. These results also support the transfer of free electrons from $Cs_3Bi_2I_9$ to TiO_2 during the generation of the $TiO_2/Cs_3Bi_2I_9/g$-C_3N_4 ternary heterojunction. Furthermore, it is noteworthy that the binding energies of Ti 2*p*, O 1*s*, and N 1*s* in the $TiO_2/$ $Cs_3Bi_2I_9/g$-C_3N_4 ternary heterojunction remain consistent with those of $TiO_2/Cs_3Bi_2I_9$ and $Cs_3Bi_2I_9/g$-C_3N_4 binary heterojunctions, respectively. These observations suggest that the transfer of free electrons in the $TiO_2/Cs_3Bi_2I_9/g$-C_3N_4 ternary heterojunction primarily occurs at the interfaces of $TiO_2/Cs_3Bi_2I_9$ and $Cs_3Bi_2I_9/g$-C_3N_4, with minimal interaction between TiO_2 and g-C_3N_4 due to the blocking layer of intermediate $Cs_3Bi_2I_9$.

3.3. Photogenerated carrier transfer and separation

The formation of the built-in electric field will promote the directed movement of the photogenerated carriers at the heterojunction interface. At the interface of $TiO_2/Cs_3Bi_2I_9$ heterojunction, although the conduction band of $Cs_3Bi_2I_9$ is higher than that of TiO_2, the built-in electric field and the energy band bending between them are not conducive to the transfer of photogenerated electrons from the conduction band of $Cs_3Bi_2I_9$ to the conduction band of TiO_2. Instead, they lead to the combination of photogenerated electrons in the conduction band of TiO_2 with the photogenerated holes in the valence band of $Cs_3Bi_2I_9$. Consequently, photogenerated carriers in the $TiO_2/Cs_3Bi_2I_9$ heterojunction are prone to undergo interfacial separation through the Z-scheme charge transfer pathway, as illustrated in Fig. 3d (III). In the case of the $Cs_3Bi_2I_9/g$-C_3N_4 heterojunction, the conduction band of $Cs_3Bi_2I_9$ is higher than that of g-C_3N_4, and the built-in electric field between them encourages the migration of photogenerated electrons in the conduction band of $Cs_3Bi_2I_9$ and photogenerated holes in the valence band of g-C_3N_4 to the g-C_3N_4 conduction band and the $Cs_3Bi_2I_9$ valence band, respectively. Consequently, the interfacial photogenerated carriers at the $Cs_3Bi_2I_9/g$-C_3N_4 interface follow the typical double-charge

transfer mode for effective separation (Fig. 3d (III)).

To ascertain the direction of photogenerated carrier migration at the heterojunction interface, *in situ* irradiated XPS (ISI-XPS) measurements [49] were performed to evaluate the binding energies of the constituent elements under both dark and illuminated conditions (Figs. S9 and S10). The variation values of the relevant elemental binding energies are summarized in Fig. 5a and b. Generally, variation in elemental binding energy is closely linked to the electron cloud density around the nucleus, where decreases and increases in binding energies correspond to the acquisition and loss of electrons around the nucleus. As depicted in Fig. 5a, when switching the dark condition to light illumination, a noticeable shift in the binding energies of Cs 3*d*, Bi 4 *f*, and I 3*d* in the $TiO_2/Cs_3Bi_2I_9$ system is observed in the direction of lower binding energies, ranging from 0.23 to 0.65 eV. Conversely, the binding energies of Ti 2*p* and O 1 *s* shift towards higher values by 0.32 to 0.40 eV, respectively. This observation suggests that light illumination brings forth respective accumulation of photogenerated electrons and holes in $Cs_3Bi_2I_9$ and TiO_2, confirming that photogenerated carrier separation at $TiO_2/Cs_3Bi_2I_9$ heterojunction interface is consistent with a Z-scheme charge transfer pathway. For the $Cs_3Bi_2I_9/g$-C_3N_4 heterojunction (Fig. 5b), all the binding energies of Cs 3*d*, Bi 4 *f* and I 3*d* under the light irradiation significantly shift in the high-energy direction by approximately 0.20 eV compared to those in the dark condition. Conversely, transitioning from the dark to the light irradiation condition results in a perceivable binding energy shift of N 1 *s* in the low-energy direction by 0.08–0.36 eV. These results indicate that photogenerated electrons and holes are enriched in g-C_3N_4 and $Cs_3Bi_2I_9$ in the $Cs_3Bi_2I_9/g$-C_3N_4 heterojunction, respectively, following a typical double-charge transfer mode.

Trapping tests employing 5,5-dimethyl-1-pyrroline *N*-oxide (DMPO) as the trapping agent were carried out to further elucidate the transfer route of photogenerated carriers in the $TiO_2/Cs_3Bi_2I_9/g$-C_3N_4 ternary heterojunction. Electron paramagnetic resonance (EPR) analysis revealed that the signal corresponding to DMPO− ·OH in the $TiO_2/$ $Cs_3Bi_2I_9$ is distinctly stronger than in pristine TiO_2 (Fig. S11a). This
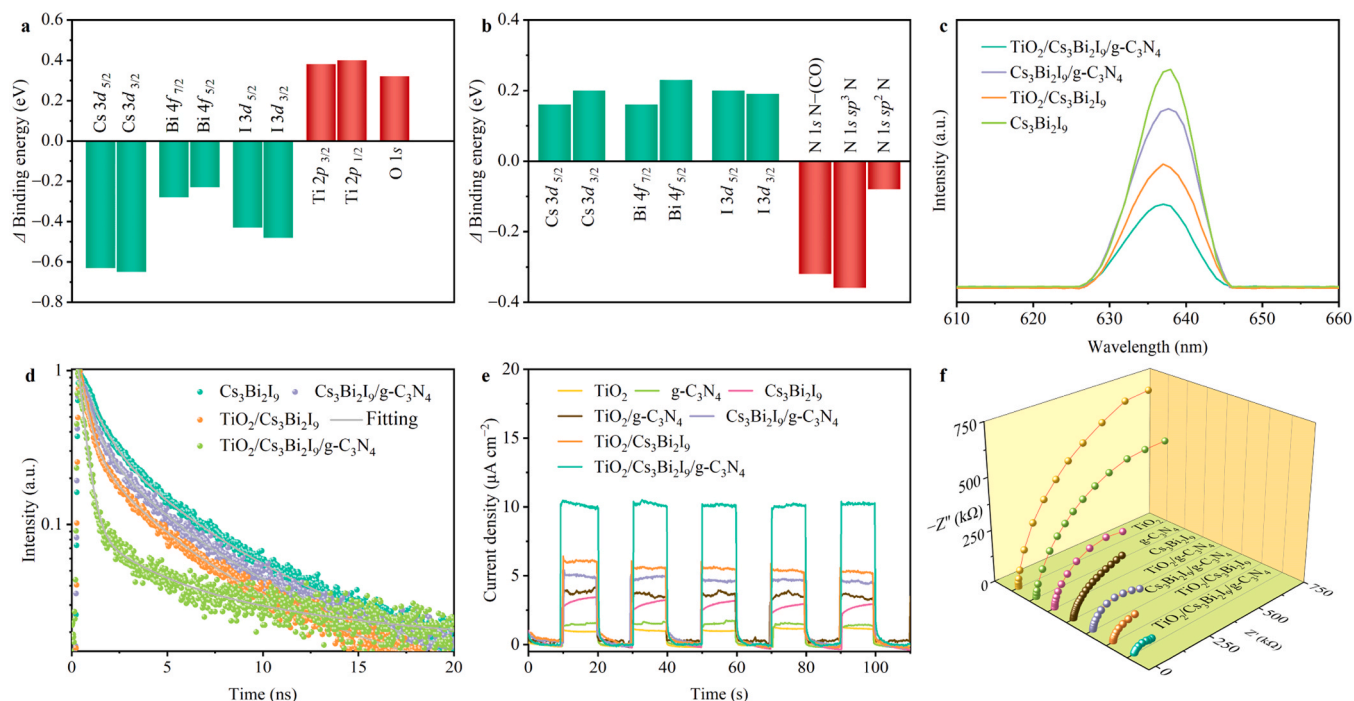
Fig. 5. a–b) Light-induced binding energy shift (Δ binding energy) in a) $TiO_2/Cs_3Bi_2I_9$ and b) $Cs_3Bi_2I_9/g-C_3N_4$ derived from ISI-XPS measurements. c–d) Steady-state PL spectra c) and time-correlated PL decay traces d) of $Cs_3Bi_2I_9$, $Cs_3Bi_2I_9/g-C_3N_4$, $TiO_2/Cs_3Bi_2I_9$ and $TiO_2/Cs_3Bi_2I_9/g-C_3N_4$. e) $I-t$ curves e) and f) EIS Nyquist plots f) of TiO_2, $g-C_3N_4$, $Cs_3Bi_2I_9$, $TiO_2/g-C_3N_4$, $Cs_3Bi_2I_9/g-C_3N_4$, $TiO_2/Cs_3Bi_2I_9$ and $TiO_2/Cs_3Bi_2I_9/g-C_3N_4$.

observation indicates that the photogenerated holes in the TiO_2 component of $TiO_2/Cs_3Bi_2I_9$ are retained rather than transferred to $Cs_3Bi_2I_9$, and photoinduced electron−hole pairs are effectively separated through electron transfer from the conduction band of TiO_2 to the valence band of $Cs_3Bi_2I_9$ with a Z-scheme mode. Additionally, both $Cs_3Bi_2I_9$ and $g-C_3N_4$ can reduce O_2 to·O_2^-, as evidenced by the characteristic signal of DMPO− ·O_2^- identified in both $Cs_3Bi_2I_9$ and $g-C_3N_4$ (Fig. S11b). Remarkably, the signal corresponding to DMPO− ·O_2^- in the $Cs_3Bi_2I_9/g-C_3N_4$ is notably stronger than in pristine $Cs_3Bi_2I_9$ and $g-C_3N_4$, indicating efficient separation of photogenerated electron−hole in $Cs_3Bi_2I_9/g-C_3N_4$. Indirect verification of the photogenerated electron transfer path between $Cs_3Bi_2I_9$ and $g-C_3N_4$ was achieved by monitoring the changes in EPR signal intensities of 2,2,6,6-tetramethylpiperidine-1-oxyl (TEMPO). The EPR pattern of TEMPO acetonitrile solution typically exhibits a triplet peak with an intensity ratio of 1:1:1 (Fig. S11c). In the absence of light irradiation, the signal intensity of TEMPO remains nearly unchanged after adding the photocatalysts. After Xe lamp irradiation for 5 min, $TiO_2/Cs_3Bi_2I_9/g-C_3N_4$ exhibits the weakest intensity of the TEMPO signal among all samples, implying that photogenerated electrons in this ternary heterojunction can be more effectively captured by TEMPO. It is noteworthy that the ternary heterojunction of $TiO_2/Cs_3Bi_2I_9/g-C_3N_4$ features a unique multi-shell hollow structure, with $Cs_3Bi_2I_9$ positioned between the layers. Consequently, when the ternary heterojunction is irradiated, photogenerated electrons in the conduction band of $Cs_3Bi_2I_9$ should flow to the conduction band of $g-C_3N_4$ through a dual charge transfer mechanism and are subsequently captured by TEMPO (Fig. S11d). Conversely, if photogenerated electrons in the conduction band of $g-C_3N_4$ flow to the valence band of $Cs_3Bi_2I_9$ via a Z-scheme transfer pathway, the photogenerated electrons in the ternary heterojunction of $TiO_2/Cs_3Bi_2I_9/g-C_3N_4$ would accumulate in the conduction band of $Cs_3Bi_2I_9$, making them less accessible to TEMPO due to $Cs_3Bi_2I_9$ being sandwiched between TiO_2 and $g-C_3N_4$.

The impact of constructing heterojunctions on the efficiency of photogenerated carrier separation was further investigated through steady-state photoluminescence (PL) measurements. The excitation wavelength of 510 nm was selected to circumvent the absorption of g-

C_3N_4 and TiO_2. As illustrated in Fig. 5c, $Cs_3Bi_2I_9$ exhibits a prominent characteristic emission peak at around 637 nm. Combining TiO_2 or $g-C_3N_4$ with $Cs_3Bi_2I_9$ to create binary composites results in a reduction in PL intensity, indicating effective charge separation at both the $TiO_2/Cs_3Bi_2I_9$ and $Cs_3Bi_2I_9/g-C_3N_4$ interfaces. Notably, the PL intensity of the $TiO_2/Cs_3Bi_2I_9/g-C_3N_4$ ternary heterojunction is further diminished compared to those of the binary heterojunctions, signifying the superior capability of the ternary heterojunction in separating photogenerated carriers. Time-resolved PL (TRPL) measurements further substantiate the favorable charge separation at the ternary heterojunction. As portrayed in Fig. 5d, the TRPL decay curve of $Cs_3Bi_2I_9$ alone represents the radiative and nonradiative processes of photogenerated excitons in $Cs_3Bi_2I_9$. By fitting the corresponding TRPL trace with a three-exponential function, the PL average lifetime of $Cs_3Bi_2I_9$ is determined to be 2.53 ns (Table S1). In comparison to $Cs_3Bi_2I_9$, the $TiO_2/Cs_3Bi_2I_9$ and $Cs_3Bi_2I_9/g-C_3N_4$ heterojunctions exhibit accelerated TRPL decay curves with PL average lifetimes of 1.63 and 1.96 ns, respectively, further indicating rapid interfacial charge transfer upon combining $Cs_3Bi_2I_9$ with TiO_2 or $g-C_3N_4$. The PL decay is even more accelerated when $Cs_3Bi_2I_9$ forms a ternary heterojunction with TiO_2 and $g-C_3N_4$, and the PL average lifetime is significantly shortened to 0.85 ns, which also confirms that ternary heterojunction featuring a double built-in electric field are highly favorable for photogenerated carrier separation.

The photocurrent response ($I-t$) and electrochemical impedance spectroscopy (EIS) measurements were further carried out to demonstrate that the ternary heterojunction favors the charge separation efficiency. As illustrated in Fig. 5e, the photocurrent densities of the $TiO_2/Cs_3Bi_2I_9$, $Cs_3Bi_2I_9/g-C_3N_4$ and $TiO_2/g-C_3N_4$ binary heterojunctions surpass those of the individual TiO_2, $Cs_3Bi_2I_9$ and $g-C_3N_4$ components. This observation underscores the role of binary heterojunctions in facilitating the separation of photogenerated carriers to some extent. Remarkably, the $TiO_2/Cs_3Bi_2I_9/g-C_3N_4$ ternary heterojunction displays the most robust photocurrent response among all the samples, further affirming the significant role played by the dual built-in electric fields within the ternary heterojunction in enhancing interface charge separation. Additionally, the results of EIS measurements on various samples

demonstrate that the impedance arc radii of the $TiO_2/Cs_3Bi_2I_9$, $Cs_3Bi_2I_9/g\text{-}C_3N_4$ and $TiO_2/g\text{-}C_3N_4$ binary heterojunction are smaller than those of the individual components, while the $TiO_2/Cs_3Bi_2I_9/g\text{-}C_3N_4$ ternary heterojunction exhibits the smallest impedance arc radius as depicted in Fig. 5f, providing clear evidence of the beneficial impact of the dual built-in electric fields on interfacial charge separation in ternary heterojunctions.

3.4. Photocatalytic activity and stability CO_2 reduction

The photocatalytic CO_2 reduction activities of ternary, binary and singlet materials were assessed utilizing a gas−solid reaction apparatus (Fig. S12) with CO_2 and water as the primary reactants. A xenon lamp was employed as the light source, and the surface temperature of the photocatalysts during the reaction process reaches up to 41.4 °C owing to the photothermal effect (Fig. S13). The results of gas chromatographic analysis revealed that the reduction products of all samples primarily consisted of CO with a selectivity of greater than 93%, accompanied by trace amounts of CH_4 (Fig. S14, Table S2). Specific yields are summarized in Fig. 6a. Both TiO_2 and $g\text{-}C_3N_4$ exhibit inferior activity of photocatalytic CO_2 reduction, yielding only 13.1 and 18.5 $\mu mol\ g^{-1}\ h^{-1}$ of CO, respectively, which should be ascribed to their weak responsiveness to photons in the visible region (Fig. 3a) and serious photogenerated carrier recombination. By combining TiO_2 and $g\text{-}C_3N_4$ to generate a $TiO_2/g\text{-}C_3N_4$ heterojunction, enhanced charge separation occurs, leading to improved photocatalytic performance with a CO yield of 51.2 $\mu mol\ g^{-1}\ h^{-1}$. Benefitting from the good light-harvesting ability, the CO

yield of $Cs_3Bi_2I_9$ can reach 38.5 $\mu mol\ g^{-1}\ h^{-1}$. Compared with the individual components, the binary heterojunctions $TiO_2/Cs_3Bi_2I_9$ and $Cs_3Bi_2I_9/g\text{-}C_3N_4$ display obviously enhanced CO yields, being 67.5 and 53.0 $\mu mol\ g^{-1}\ h^{-1}$, respectively, which can be attributed to the improved separation of photogenerated carriers by the formation of the heterojunction. Notably, the photocatalytic CO_2 reduction activity of ternary heterojunction $TiO_2/Cs_3Bi_2I_9/g\text{-}C_3N_4$ significantly exceeds those of the binary heterojunction, and its CO yield reaches up to 120.6 μmol $g^{-1}\ h^{-1}$, which suggests that the presence of double in-built electric fields within the ternary heterojunction are favorable for improving the separation efficiency of the photogenerated carriers.

Furthermore, the long-term photocatalytic activities of all samples were evaluated under the identical conditions to affirm the advantage of the multi-shell hollow structure in terms of stability, and the results are presented in Fig. 6b. The photocatalytic CO_2 reduction activity of individual $Cs_3Bi_2I_9$ exhibits a significant decline after 25 h, due to the propensity of $Cs_3Bi_2I_9$ to decompose in a water-containing environment. Although TiO_2 and $g\text{-}C_3N_4$ exhibit poor activity for photocatalytic CO_2 reduction, but they possess good stability. This inherent stability extends to the $TiO_2/g\text{-}C_3N_4$ heterojunction as well. Combining $Cs_3Bi_2I_9$ with TiO_2 or $g\text{-}C_3N_4$ to form heterojunctions can effectively improve the photocatalytic activity, but can not improve the stability, which should be caused by the fact that $Cs_3Bi_2I_9$ in the binary heterojunctions are still directly exposed to water vapor. It is noted that the ternary heterojunction $TiO_2/Cs_3Bi_2I_9/g\text{-}C_3N_4$ exhibits not only an improved photocatalytic activity, but also exceptional photocatalytic stability. The photocatalytic activity remains unimpaired even after more than of

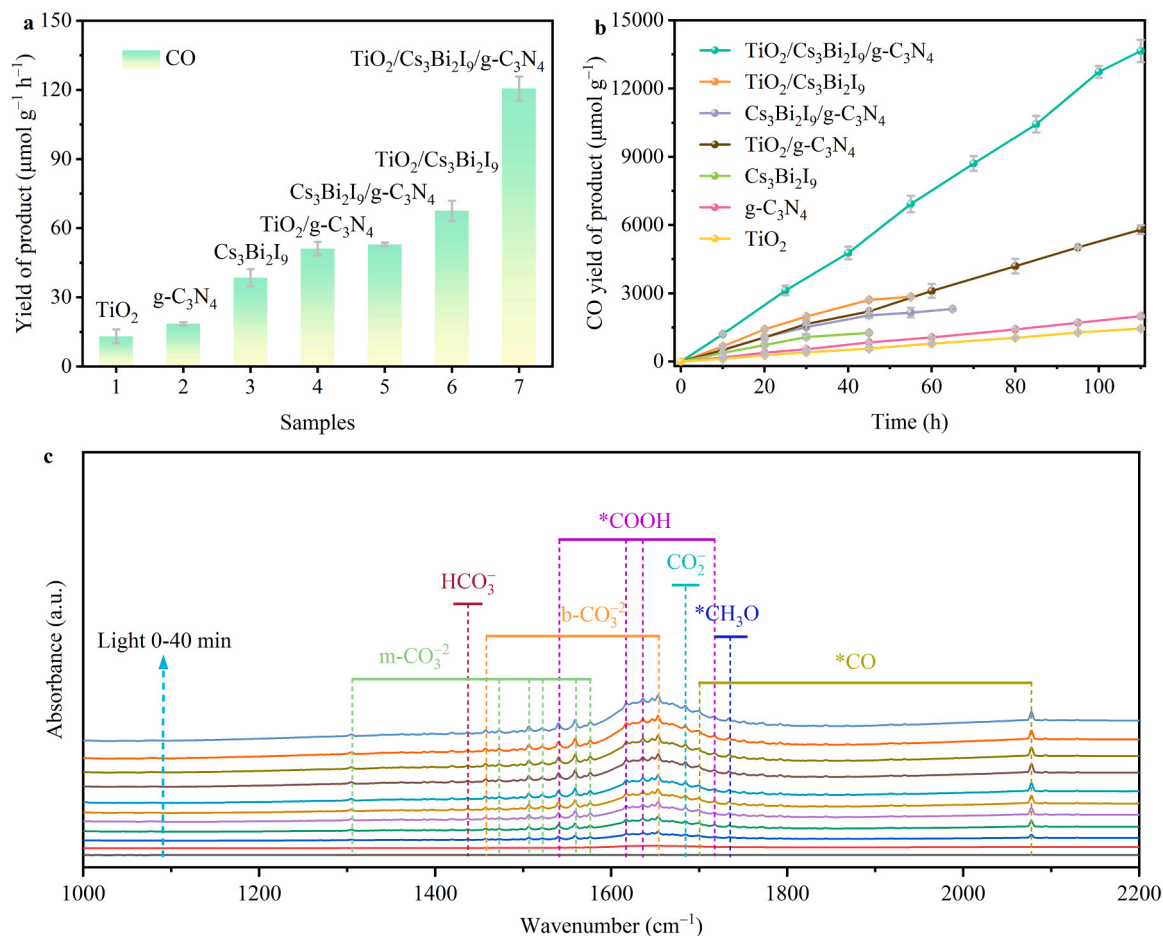**Fig. 6.** a) The CO generation rates under irradiation of 10 h and b) CO production during the long-term photocatalytic CO_2 reduction with TiO_2, $g\text{-}C_3N_4$, $Cs_3Bi_2I_9$, $TiO_2/g\text{-}C_3N_4$, $Cs_3Bi_2I_9/g\text{-}C_3N_4$, $TiO_2/Cs_3Bi_2I_9$ and $TiO_2/Cs_3Bi_2I_9/g\text{-}C_3N_4$ as the photocatalysts. c) *In situ* FTIR spectra for photocatalytic CO_2 reduction over $TiO_2/Cs_3Bi_2I_9/g\text{-}C_3N_4$.

continuous light exposure. Meanwhile, a continuously increasing amount of CH_4 (6.2 µmol g^{-1} h^{-1}, Fig. S15) and a stoichiometric ratio of O_2 (72.7 µmol g^{-1} h^{-1}, Fig. S16) can also been identified by the gas chromatography measurements. The excellent stability of TiO$_2$/Cs$_3$Bi$_2$I$_9$/g-C$_3$N$_4$ should be attributed to the unique sandwich structure that prevents direct exposure of Cs$_3$Bi$_2$I$_9$ to water vapor environment. In this multi-shell hollow structure, the CO_2 reduction and water oxidation half-reactions occur on the surfaces of g-C$_3$N$_4$ and TiO$_2$ surfaces, respectively, while Cs$_3$Bi$_2$I$_9$ primarily functions as a light absorber.

The XRD pattern of TiO$_2$/Cs$_3$Bi$_2$I$_9$/g-C$_3$N$_4$ after the photocatalytic reaction further confirms that the crystal structure remained intact (Fig. S17), where the characteristic diffraction peaks still closely match with the standard pattern of JCPDS 73−0707 for Cs$_3$Bi$_2$I$_9$. Additionally, TiO$_2$/Cs$_3$Bi$_2$I$_9$/g-C$_3$N$_4$ after the photocatalytic reaction still maintains its original hollow microsphere structure as demonstrated by TEM measurement (Fig. S18). These results validate that ternary heterojunction TiO$_2$/Cs$_3$Bi$_2$I$_9$/g-C$_3$N$_4$ has an excellent stability in the gas−solid reaction system. In contrast, the characteristic diffraction peaks of Cs$_3$Bi$_2$I$_9$ in TiO$_2$/Cs$_3$Bi$_2$I$_9$ and Cs$_3$Bi$_2$I$_9$/g-C$_3$N$_4$ have essentially disappeared after the photocatalytic reaction, exposing only the characteristic peaks of TiO$_2$ and g-C$_3$N$_4$ that were originally obscured (Fig. S19). In the case of these binary heterojunctions, Cs$_3$Bi$_2$I$_9$ remains in direct contact with water vapor and undergoes gradual degradation, indicating that constructing binary heterojunction cannot enhance the stability of Cs$_3$Bi$_2$I$_9$-based materials in the system containing water.

A series of reference experiments were conducted to elucidate the sources of reduction and oxidation products with TiO$_2$/Cs$_3$Bi$_2$I$_9$/g-C$_3$N$_4$ as a photocatalyst. As depicted in Fig. S20, no products were detected in the absence of light irradiation or photocatalyst, implying that the reduction of CO_2 is initiated by light exposure on the photocatalyst. Furthermore, a control experiment conducted without the presence of water vapor also demonstrated negligible generation of CO, suggesting that the source of electrons for CO_2 photoreduction is derived from water oxidation. These deductions were further corroborated through isotopically labeled experiments with $^{13}CO_2$ and $H_2^{18}O$ as feedstocks. In the $^{13}CO_2$ isotope tracing experiment, major mass spectrum signals belonged to ^{13}CO ($m/z = 29$) and $^{13}CH_4$ ($m/z = 17$) can be observed (Fig. S21), unequivocally indicating that both CO and CH$_4$ products originate from the CO_2 conversion. Additionally, the result of mass spectrometry analyses from the $H_2^{18}O$ isotope tracing experiment (Fig. S22) clearly identified a distinct signal at $m/z = 36$, corresponding to $^{18}O_2$, proving conclusive evidence that the O_2 product indeed stems from water oxidation.

Furthermore, *in situ* diffuse reflectance infrared Fourier transformation spectroscopy measurement was performed to investigate the photocatalytic CO_2 reduction reaction pathway, allowing for the analysis of reaction intermediates involved in the CO_2 reduction process. To establish a reference background, the air in the test system was substituted with a continuous supply of argon gas. As presented in Fig. 6c, characteristic signals of the intermediates could not be detected during the pre-illumination period. Upon exposure to light, these characteristic signals of intermediates emerged at various time intervals as CO_2 was continuously bubbled in the aqueous solution. A suite of signal peaks appeared in the range of 1300–1800 cm^{-1} with increasing light exposure. Specifically, signal peaks at 1305, 1473, 1506, 1521, 1559 and 1576 cm^{-1} can be attributed to the characteristic vibrations of monodentate carbonate (m-CO_3^{2-}) [50,51]. Signal peaks at 1457 and 1654 cm^{-1} correspond to the characteristic vibration of bidentate carbonate (b-CO_3^{2-}) [51,52]. The characteristic peak at 1436 cm^{-1} is assigned to the HCO_3^- [53]. Importantly, distinct signal peaks at 1541, 1617, 1636 and 1718 cm^{-1} were identified as characteristic features of *COOH [50,52,54,55], which is a crucial intermediate in the conversion of CO_2 to CO. Additionally, significant signals at 1699 and 2079 cm^{-1} were detected, which are associated with the *CO intermediate absorbed on the catalyst surface [55,56]. Furthermore, the signal peak at 1735 cm^{-1} can be attributed to *CH$_3$O [54], which is a key intermediate

in CH$_4$ formation. Based on these results, we can propose a reaction pathway for the photocatalytic CO_2 reduction over TiO$_2$/Cs$_3$Bi$_2$I$_9$/g-C$_3$N$_4$. Initially, the photocatalyst TiO$_2$/Cs$_3$Bi$_2$I$_9$/g-C$_3$N$_4$ absorbs photons, generating electron-hole pairs. Subsequently, the photogenerated carriers achieve efficient charge separation by the action of double built-in electric fields, leading to the accumulation of photogenerated electrons and holes in g-C$_3$N$_4$ and TiO$_2$, respectively. Thereafter, photogenerated electrons in the g-C$_3$N$_4$ conduction band trigger the reduction reaction of CO_2 via the proton-coupled electron transfer pathway, resulting in the formation of intermediates such as *COOH, *CO, and *CH$_3$O. These intermediates further produce CO and CH$_4$ via proton-coupled electron transfer reactions as illustrated in Fig. S23. Meanwhile, photogenerated holes in the valence band of TiO$_2$ initiate the oxidation of H_2O, generating O_2 and providing a proton source for CO_2 reduction.

4. Conclusion

To summarize, we have effectively demonstrated a strategy for simultaneously enhancing the stability and activity of halide perovskite-based photocatalyst for artificial photosynthesis by establishing a ternary heterojunction. A lead-free halide perovskite-based ternary heterojunction of TiO$_2$/Cs$_3$Bi$_2$I$_9$/g-C$_3$N$_4$ with a multi-shell hollow structure was successfully constructed using a template method of continuous deposition combined with *in situ* conversion. The incorporation of double in-built electric fields within the ternary heterojunction can effectively enhance the separation efficiency and maintain the oxidation potential of photogenerated carriers, leading to a substantial improvement in photocatalytic activity for overall artificial photosynthesis reaction. What is more, the two-sided protection of TiO$_2$ and g-C$_3$N$_4$ remarkably ameliorate the photocatalytic stability in a water-contained system. The presented strategy for constructing a ternary heterojunction opens up a new window for the design of efficient and stable halide perovskite photocatalysts for energy conversion. We anticipate that notable efficiency improvement in stable halide perovskite based photocatalyst could be achieved in the near future, via elaborate selection of high-activity protective layers and modulation of interfacial engineering.

CRediT authorship contribution statement

Feng You-Xiang: Writing – original draft, Methodology, Investigation. **Su Ke:** Investigation. **Liu Zhao-Lei:** Investigation. **Yuan Su-Xian:** Investigation. **Zhang Min:** Writing – review & editing, Supervision, Methodology, Funding acquisition, Conceptualization. **Lu Tong-Bu:** Writing – review & editing, Supervision, Funding acquisition, Conceptualization. **Mu Yan-Fei:** Methodology.

Declaration of Competing Interest

The authors declare that they have no known competing financial interests or personal relationships that could have appeared to influence the work reported in this paper.

Data availability

Data will be made available on request.

Appendix A. Supporting information

Supplementary data associated with this article can be found in the online version at doi:10.1016/j.apcatb.2024.123821.

References

[1] S. Fang, M. Rahaman, J. Bharti, E. Reisner, M. Robert, G.A. Ozin, Y.H. Hu, Photocatalytic CO_2 reduction, Nat. Rev. Methods Prim. 3 (2023) 61.

[2] H. Lin, S. Luo, H. Zhang, J. Ye, Toward solar-driven carbon recycling, Joule 6 (2022) 294–314.

[3] T. Wang, J. Gong, Sacrificing nothing to reduce CO_2, Nat. Energy 5 (2020) 642–643.

[4] M. Zhang, J. Zhang, P. Wang, A bifunctional photocatalyst boosts resourceful utilization of CO_2, Matter 6 (2023) 2530–2532.

[5] S. Ye, C. Ding, M. Liu, A. Wang, Q. Huang, C. Li, Water oxidation catalysts for artificial photosynthesis, Adv. Mater. 31 (2019) 1902069.

[6] K. Kosugi, C. Akatsuka, H. Iwami, M. Kondo, S. Masaoka, Iron-complex-based supramolecular framework catalyst for visible-light-driven CO_2, Reduct., J. Am. Chem. Soc. 145 (2023) 10451–10457.

[7] Y. Kamakura, C. Suppaso, I. Yamamoto, R. Mizuochi, Y. Asai, T. Motohashi, D. Tanaka, K. Maeda, Tin(II)-based metal–organic frameworks enabling efficient, selective reduction of CO_2 to formate under visible light, Angew. Chem. Int. Ed. 62 (2023) e202305923.

[8] Q. Zhang, S. Gao, Y. Guo, H. Wang, J. Wei, X. Su, H. Zhang, Z. Liu, J. Wang, Designing covalent organic frameworks with Co-O$_4$ atomic sites for efficient CO_2 photoreduction, Nat. Common 14 (2023) 1147.

[9] B. Yu, T. Meng, X. Ding, X. Liu, H. Wang, B. Chen, T. Zheng, W. Li, Q. Zeng, J. Jiang, Hydrogen-bonded organic framework ultrathin nanosheets for efficient visible-light photocatalytic CO_2 reduction, Angew. Chem. Int. Ed. 61 (2022) e202211482.

[10] A.C. Ghosh, A. Legrand, R. Rajapaksha, G.A. Craig, C. Sassoye, G. Balázs, D. Farrusseng, S. Furukawa, J. Canivet, F.M. Wisser, Rhodium-based metal−organic polyhedra assemblies for selective CO_2 photoreduction, J. Am. Chem. Soc. 144 (2022) 3626–3636.

[11] J. Li, H. Huang, W. Xue, K. Sun, X. Song, C. Wu, L. Nie, Y. Li, C. Liu, Y. Pan, H.-L. Jiang, D. Mei, C. Zhong, Self-adaptive dual-metal-site pairs in metal-organic frameworks for selective CO_2 photoreduction to CH_4, Nat. Catal. 4 (2021) 719–729.

[12] F. Arcudi, L. Đorđevic, B. Nagasing, S. I, E.A. Weiss, Quantum dot-sensitized photoreduction of CO_2 in water with turnover number > 80000, J. Am. Chem. Soc. 143 (2021) 18131–18138.

[13] H. Yuan, B. Cheng, J. Lei, L. Jiang, Z. Han, Promoting photocatalytic CO_2 reduction with a molecular copper purpurin chromophore, Nat. Common 12 (2021) 1835.

[14] W. Soontornchaiyakul, S. Yoshino, T. Kanazawa, R. Haruki, D. Fan, S. Nozawa, Y. Yamaguchi, A. Kudo, CH_4 synthesis from CO_2 and H_2O of an electron source over Rh–Ru cocatalysts loaded on NaTaO$_3$:Sr photocatalysts, J. Am. Chem. Soc. 145 (2023) 20485–20491.

[15] P.M. Ismail, S. Ali, S. Ali, J. Li, M. Liu, D. Yan, F. Raziq, F. Wahid, G. Li, S. Yuan, X. Wu, J. Yi, J.S. Chen, Q. Wang, L. Zhong, Y. Yang, P. Xia, L. Qiao, Photoelectron "bridge" in Van Der Waals heterojunction for enhanced photocatalytic CO_2 conversion under visible light, Adv. Mater. 35 (2023) 2303047.

[16] H.A.E. Omr, R. Putikam, M.K. Hussien, A. Sabbah, T.-Y. Lin, K.-H. Chen, H.-L. Wu, S.-P. Feng, M.-C. Lin, H. Lee, Design of sculptured SnS/g-C_3N_4 photocatalytic nanostructure for highly efficient and selective CO_2 conversion to methane, Appl. Catal. B 324 (2023) 122231.

[17] S. Hu, P. Qiao, X. Yi, Y. Lei, H. Hu, J. Ye, D. Wang, Selective photocatalytic reduction of CO_2 to CO mediated by silver single atoms anchored on tubular carbon nitride, Angew. Chem. Int. Ed. 62 (2023) e202304585.

[18] Y. Shen, C. Ren, L. Zheng, X. Xu, R. Long, W. Zhang, Y. Yang, Y. Zhang, Y. Yao, H. Chi, J. Wang, Q. Shen, Y. Xiong, Z. Zou, Y. Zhou, Room-temperature photosynthesis of propane from CO_2 with Cu single atoms on vacancy-rich TiO_2, Nat. Common. 14 (2023) 1117.

[19] Y. Zhang, B. Johannessen, P. Zhang, J. Gong, J. Ran, S.-Z. Qiao, Reversed electron transfer in dual single atom catalyst for boosted photoreduction of CO_2, Adv. Mater. 35 (2023) 2306923.

[20] J. Zhou, J. Li, L. Kan, L. Zhang, Q. Huang, Y. Yan, Y. Chen, J. Liu, S.-L. Li, Y.-Q. Lan, Linking oxidative and reductive clusters to prepare crystalline porous catalysts for photocatalytic CO_2 reduction with H_2O, Nat. Common 13 (2022) 4681.

[21] L. Xiong, Y. Hu, Y. Wang, W. Dong, X. Zhang, K. Zhang, T. Wang, J. Shen, Y. Yang, S bridging active centers coordination with oxygen vacancy of metastable blue WO_3 for efficient C–C coupling and highly selective photoconversion CO_2 to ethylene, Appl. Catal. B 340 (2024) 123263.

[22] H. Huang, R. Shi, Z. Li, J. Zhao, C. Su, T. Zhang, Triphase photocatalytic CO_2 reduction over silver-decorated titanium oxide at a gas−water boundary, Angew. Chem. Int. Ed. 61 (2022) e202200802.

[23] E. Gong, S. Ali, C.B. Hiragond, H.S. Kim, N.S. Powar, D. Kim, H. Kim, S.-I. In, Solar fuels: research and development strategies to accelerate photocatalytic CO_2 conversion into hydrocarbon fuels, Energy Environ. Sci. 15 (2022) 880–937.

[24] Z.-Y. Chen, N.-Y. Huang, Q. Xu, Metal halide perovskite materials in photocatalysis: design strategies and applications, Coord. Chem. Rev. 481 (2023) 215031.

[25] J. Wang, Y. Shi, Y. Wang, Z. Li, Rational design of metal halide perovskite nanocrystals for photocatalytic CO_2 reduction: recent advances, challenges, and prospects, ACS Energy Lett. 7 (2022) 2043–2059.

[26] Q.A. Akkerman, G. Rainò, M.V. Kovalenko, L. Manna, Genesis, challenges and opportunities for colloidal lead halide perovskite nanocrystals, Nat. Mater. 17 (2018) 394–405.

[27] M.V. Kovalenko, L. Protesescu, M.I. Bodnarchuk, Properties and potential optoelectronic applications of lead halide perovskite nanocrystals, Science 358 (2017) 745–750.

[28] H. Huang, D. Verhaeghe, B. Weng, B. Ghosh, H. Zhang, J. Hofkens, J.A. Steele, M.B. J. Roeffaers, Metal halide perovskite based heterojunction photocatalysts, Angew. Chem. Int. Ed. 61 (2022) e202203261.

[29] Q.-M. Sun, J.-J. Xu, F.-F. Tao, W. Ye, C. Zhou, J.-H. He, J.-M. Lu, Boosted inner surface charge transfer in perovskite nanodots@mesoporous titania frameworks for efficient and selective photocatalytic CO_2 reduction to methane, Angew. Chem. Int. Ed. 61 (2022) e202200872.

[30] F. Xu, K. Meng, B. Cheng, S. Wang, J. Xu, J. Yu, Unique S-scheme heterojunctions in self-assembled TiO_2/CsPbBr$_3$ hybrids for CO_2 photoreduction, Nat. Commun. 11 (2020) 4613.

[31] H. Huang, J. Zhao, Y. Du, C. Zhou, M. Zhang, Z. Wang, Y. Weng, J. Long, J. Hofkens, J.A. Steele, M.B.J. Roeffaers, Direct Z-scheme heterojunction of semicoherent FAPbBr$_3$/Bi$_2$WO$_6$ interface for photoredox reaction with large driving force, ACS Nano 14 (2020) 16689–16697.

[32] Y. Jiang, J.-F. Liao, H.-Y. Chen, H.-H. Zhang, J.-Y. Li, X.-D. Wang, D.-B. Kuang, All-solid-state Z-scheme α-Fe$_2$O$_3$/amine-RGO/CsPbBr$_3$ hybrids for visible-light-driven photocatalytic CO_2 reduction, Chem 6 (2020) 766–780.

[33] J.T. DuBose, P.V. Kamat, Efficacy of perovskite photocatalysis: challenges to overcome, ACS Energy Lett. 7 (2022) 1994–2011.

[34] R. Cheng, Z.-B. Liang, L. Zhu, H. Li, Y. Zhang, C.-F. Wang, S. Chen, Fibrous nanoreactors from microfluidic blow spinning for mass production of highly stable ligand-free perovskite quantum dots, Angew. Chem. Int. Ed. 61 (2022) e202204371.

[35] Y.-F. Xu, X.-D. Wang, J.-F. Chen, B.-X. Liao, H.-Y. Chen, D.-B. Kuang, Amorphous-TiO_2-encapsulated CsPbBr$_3$ nanocrystal composite photocatalyst with enhanced charge separation and CO_2 fixation, Adv. Mater. Interfaces 5 (2018) 1801015.

[36] M. Ou, W. Tu, S. Yin, W. Xing, S. Wu, H. Wang, S. Wan, Q. Zhong, R. Xu, Amino-assisted anchoring of CsPbBr$_3$ perovskite quantum dots on porous g-C_3N_4 for enhanced photocatalytic CO_2 reduction, Angew. Chem. Int. Ed. 57 (2018) 13570–13574.

[37] C. Wang, F. Wang, Z. Liu, Y. Zhao, Y. Liu, Q. Yue, H. Zhu, Y. Deng, Y. Wu, D. Zhao, N-doped carbon hollow microspheres for metal-free quasi-solid-state full sodium-ion capacitors, Nano Energy 41 (2017) 674–680.

[38] J. Wang, X. Wang, Q. Chen, H. Xu, M. Dai, M. Zhang, W. Wang, H. Song, Microstructural modification of hollow TiO_2 nanospheres and their photocatalytic performance, Appl. Surf. Sci. 535 (2021) 147641.

[39] J. Pan, Z. Dong, B. Wang, Z. Jiang, C. Zhao, J. Wang, C. Song, Y. Zheng, C. Li, The enhancement of photocatalytic hydrogen production via Ti^{3+} self-doping black TiO_2/g-C_3N_4 hollow core-shell nano-heterojunction, Appl. Catal. B 242 (2019) 92–99.

[40] Y.-X. Feng, G.-X. Dong, K. Su, Z.-L. Liu, W. Zhang, M. Zhang, T.-B. Lu, Self-template-oriented synthesis of lead-free perovskite Cs$_3$Bi$_2$I$_9$ nanosheets for boosting photocatalysis of CO_2 reduction over Z-scheme heterojunction Cs$_3$Bi$_2$I$_9$/CeO$_2$, J. Energy Chem. 69 (2022) 348–355.

[41] Z. Hu, K. Li, X. Wu, N. Wang, X. Li, Q. Li, L. Li, K. Lv, Dramatic promotion of visible-light photoreactivity of TiO_2 hollow microspheres towards NO oxidation by introduction of oxygen vacancy, Appl. Catal. B 256 (2019) 117860.

[42] M. Liu, C. Wei, H. Zhuzhang, J. Zhou, Z. Pan, W. Lin, Z. Yu, G. Zhang, X. Wang, Fully condensed poly (triazine imide) crystals: extended π-conjugation and structural defects for overall water splitting, Angew. Chem. Int. Ed. 61 (2022) e202113389.

[43] F. Tian, Y. Zhang, J. Zhang, C. Pan, Raman spectroscopy: a new approach to measure the percentage of anatase TiO_2 exposed (001) facets, J. Phys. Chem. C 116 (2012) 7515–7519.

[44] J. Wang, Y. Li, L. Ma, JC. Shen, Q. Yang, Air-stabilized lead-free hexagonal Cs$_3$Bi$_2$I$_9$ nanocrystals for ultrahigh-performance optical detection, Adv. Funct. Mater. 32 (2022) 2203072.

[45] Y. Tang, X. Wang, J. Chen, X. Wang, D. Wang, Z. Mao, Templated transformation of g-C_3N_4 nanosheets into nitrogen-doped hollow carbon sphere with tunable nitrogen-doping properties for application in Li-ions batteries, Carbon 168 (2020) 458–467.

[46] K. Su, S.X. Yuan, L.Y. Wu, Z.L. Liu, M. Zhang, T.B. Lu, Nanoscale Janus Z-scheme heterojunction for boosting artificial photosynthesis, Small 19 (2023) 2301192.

[47] Z.-L. Liu, R.-R. Liu, Y.-F. Mu, Y.-X. Feng, G.-X. Dong, M. Zhang, T.-B. Lu, In situ construction of lead-free perovskite direct Z-scheme heterojunction Cs$_3$Bi$_2$I$_9$/Bi$_2$WO$_6$ for efficient photocatalysis of CO_2 reduction, Sol. RRL 5 (2021) 2000691.

[48] J.-H. Zhang, J. Yang, M. Zhang, H.-J. Wang, R. Si, D.-C. Zhong, T.-B. Lu, Metal-organic layers as a platform for developing single-atom catalysts for photochemical CO_2 reduction, Nano Energy 80 (2021) 105542.

[49] J. Low, B. Dai, T. Tong, C. Jiang, J. Yu, In situ irradiated X-ray photoelectron spectroscopy investigation on a direct Z-scheme TiO_2/CdS composite film photocatalyst, Adv. Mater. 31 (2018) 1802981.

[50] Y. Zhang, X. Zhi, J.R. Harmer, H. Xu, K. Davey, J. Ran, S.-Z. Qiao, Facet-specific active surface regulation of Bi$_x$MO$_y$ (M=Mo, V, W) nanosheets for boosted photocatalytic CO_2 reduction, Angew. Chem. Int. Ed. 61 (2022) e202212355.

[51] L. Liu, Y. Jiang, H. Zhao, J. Chen, J. Cheng, K. Yang, Y. Li, Engineering coexposed {001} and {101} facets in oxygen-deficient TiO_2 nanocrystals for enhanced CO_2 photoreduction under visible light, ACS Catal. 6 (2016) 1097–1108.

[52] G. Zhou, J. Yang, X. Zhu, Q. Li, Q. Yu, W. El-alami, C. Wang, Y. She, J. Qian, H. Xu, H. Li, Cryo-induced closely bonded heterostructure for effective CO_2 conversion: the case of ultrathin BP nanosheets/g-C_3N_4, J. Energy Chem. 49 (2020) 89–95.

[53] K. Wang, Z. Hu, P. Yu, A.M. Balu, K. Li, L. Li, L. Zeng, C. Zhang, R. Luque, K. Yan, H. Luo, Understanding bridging sites and accelerating quantum efficiency for photocatalytic CO_2 reduction, Nano-Micro Lett. 16 (2024) 5.

[54] S. Barman, A. Singh, F.A. Rahimi, T.K. Maji, Metal-free catalysis: a redox-active donor−acceptor conjugated microporous polymer for selective visible-light-driven CO_2 reduction to CH_4, J. Am. Chem. Soc. 143 (2021) 16284–16292.

[55] N. Li, X.-P. Zhai, B. Ma, H.-J. Zhang, M.-J. Xiao, Q. Wang, H.-L. Zhang, Highly selective photocatalytic CO_2 reduction via a lead-free perovskite/MOF catalyst, J. Mater. Chem. A. 11 (2023) 4020–4029.

[56] Y. Wang, K. Wang, J. Meng, C. Ban, Y. Duan, Y. Feng, S. Jing, J. Ma, D. Yu, L. Gan, X. Zhou, Constructing atomic surface concaves on Bi_5O_7Br nanotube for efficient photocatalytic CO_2 reduction, Nano Energy 109 (2023) 108305.